Single-gene tuning of cell cycle period and noise, swarming motility and surface adhesion

Yihan Lin[1, 4], Sean Crosson[2, 3*], and Norbert F. Scherer[1, 4, *]
Departments of [1]Chemistry, [2]Biochemistry and Molecular Biology, [3]The Committee on Microbiology, and [4]Institute for Biophysical Dynamics,
University of Chicago, Chicago, IL 60637
* scrosson@uchicago.edu and nfschere@uchicago.edu

Supplementary Information

Table of Contents

Supplementary Methods

More Details on Microscope Configurations

The differences in microscope configurations for fluorescence and non-fluorescence measurements are described as following. For experiments with DivJ-EGFP, a high numerical aperture oil objective (Plan APO 60X N.A. 1.4, Nikon Instrument, Melville, NY) was used to perform objective-based total internal reflection fluorescence (TIRF) microscopy. With an additional 4X eyepiece expander (Nikon Instrument, Austin, TX), the total magnification is 240X. The laser beam, reflected by a dichroic mirror (FF500/646-Di01, Semrock, Rochester, NY), was directed to the coverslip-water interface at the critical reflection angle with a relatively low incident power of 0.3 mW (corresponds to ~ 20 W/cm^2 out of the objective). The fluorescence emission passed through a band pass filter (HQ525/50, Chroma Technology, Rockingham, VT) and was imaged onto a back-illuminated EMCCD (iXon DV887-BI, Andor Technology, South Windsor, CT) with 1 sec exposure time and 200 EM gain. The fluorescence image (512 pixels X 512 pixels in size corresponds to a 34 μm X 34μm area) was taken once every five minutes while the bright-field DIC image of the same area was taken at 1/min frame rate. For autofocusing, we used the position information of the back reflected beam of another TIR-aligned 633 nm laser (LHRP-0081, Research Electro-Optics, Boulder, CO) as the continuous feedback for the adjustment of objective motor allowing focus stabilization with up to 50 nm precision. For experiments with strains where DivJ does not have EGFP tag, a long working-distance objective (LUCPLFLN 40X N.A. 0.6, Olympus America, Center Valley, PA) was used to prevent heat loss through the objective. The total magnification was 60X with the use of an additional 1.5X slider in the microscope. A conventional bright-filed image was captured by a monochrome CCD (LCL-902C, Watec Inc, Orangeburg, NY) with 50 ms exposure time (a size of 640 pixels X 480 pixels corresponding to a 90 μm X 78 μm area) at a frame rate of 1/min. Focus measures [1] calculated from bright-field images were used as criteria for autofocusing.

Image Processing and Data Analysis

For analysis of the data from non-fluorescent construct, regular bright-field images (1 frame per min) for each experiment were loaded as a stack into ImageJ, thresholded, and analyzed with object analyzer to obtain the growth curves in Figure 5B. This analysis relies on the threshold brightness level for defining the cell bodies as well as the threshold pixel number for defining an object (i.e. a cell), and we chose both thresholds manually for each stack of images by comparing the thresholded stack and the original stack. The stalked cell cycle is defined as the time difference between two successive divisions of the stalked cell. The swarmer cell cycle is the time difference between its initial attachment to the surface and its first division. These times were analyzed manually for individual bacteria and statistics are obtained as in Figure 2B. To analyze division time statistics for the *divJ*::Tn5 mutant strain which has a noisy genetic background [2], we only characterized cells with length less than about four times that of the wild-type cells since most filamentous cells tend to grow out of the surface and out of the field of view. The swarmer cell adhesion frequency is calculated by the number of surface adhered swarmer cells over the total number of new born swarmer cells. The filament fraction is defined by percentage of cells that become filamented within 3hrs of

appearance, i.e. number of cells that turn into the filament form within 3 hrs of appearance divided by the total number of cells tracked. We restricted this analysis to a 3 hr period for each cell because the high surface density that occurs at later times under some conditions does not allow long time tracking of individual cells.

For analysis of images from the fluorescent construct, the fluorescent images (16-bit, 1 frame every 5 min) were first loaded into ImageJ (NIH, Bethesda, MD) as a stack and were processed with the non-uniform background subtraction plugin for initial background subtraction. With ImageJ ROI tool, three rectangular boxes were manually drawn for each individual cell: to define the signal from the lateral membrane (excluding the stalked pole), the stalked pole, and the background area near each cell for successive frames. It should be noted that not all images are well focused (partially due to the inefficiency of the autofocusing system) and therefore only the sharp focused images are included in this analysis. The image stack and the ROI information are imported and processed with Matlab (Mathworks, Natick, MA) to obtain intensities of each area (membrane, stalked pole, and background area), defined as the average of the five brightest pixels inside each area. The background intensity was subtracted from the lateral membrane and stalked intensities to yield traces as shown (Figure 7C, Figure S5). For the steady-state intensities shown in Figure 7F, fluorescence image obtained after 6hrs of induction for each stack is used to calculate individual cells' lateral membrane and stalked intensities. Note that for steady state analysis, only cells within the center of the illumination (i.e. center of the laser profile) were included. For the analysis of integrated intensity that is used for quantitative comparison between experiment and simulation (i.e. Figure S7A), stalked cells that just divided are used to calculate the integrated intensities for both stalked and lateral membrane regions.

Deterministic Simulation of the Simplified *Caulobacter* Network

We include five components (CtrA, CtrA~P, DivK, DivK~P, DivJ) in our simulation of a simplified network for the stalked cell cycle of *Caulobacter* (Figure 3A) and to model the oscillatory behaviors of these proteins along the ~ 60 min cycle period (experimental stalked cell cycle time in microfluidics ([2] and our experiment)). We do not try to describe the detailed cellular processes controlled by regulatory proteins and the feedback signals from these processes as in [3]. Instead we focus on the production, phosphorylation, and the degradation mechanisms leading to the oscillation of CtrA (and its active form CtrA~P). Protein-level modeling is employed with the assumption that the production profile of each protein follows its mRNA profile [4], which is justified for CtrA and DivK [5-6]. We also employ a Hill-function model for activation and inhibition of promoter expression as in [3-4, 7] with Hill coefficients $n = 2$. For phosphorylation, dephosphorylation, and degradation, we apply first-order reaction rate constants for these processes defined by their half-life times. The differential equations governing the concentration evolution of each protein are listed in Table S2 and the explanations of each parameter value as well as the values of initial conditions and thresholds are included in Table S3. The source code (Matlab) is included as a supplement to the manuscript. The detailed mechanisms of the modeling for each protein are described as follows.

CtrA **:** Two promoters *ctrA* P1 and *ctrA* P2, with temporally regulated activities, are responsible for the production of CtrA in the cell cycle [8]. After the chromosome is

hemi-methylated, the P1 promoter is activated by the signal from GcrA, another regulatory protein whose expression is initiated at the beginning of the stalk cell cycle [9-10], and is repressed by phosphorylated CtrA [8] as well as full-methylation of the chromosome at the later cell cycle stage. In modeling the production of CtrA from the P1 promoter, two simplifications are made: (1) since concentration variation of GcrA is fairly small in the early stalk cell [10] where P1 activity peaks, we assume a constant signal of activation from GcrA and do not consider the GcrA concentration oscillation; (2) we do not consider the methylation state of the chromosome, which regulates the activity of the P1 promoter and assume that the P1 promoter quickly becomes hemi-methylated and active after the beginning of each stalk cycle. For the modeling of the stronger promoter, the P2 promoter whose activity is initiated by the accumulating CtrA~P and peaks at the late predivisional cell [8], we assume a large binding constant between CtrA~P and its P2 promoter ($K_{bd,ctra2}$ = 9000 nM) in the Hill function to account for the late activation of this promoter. Relatively high activities are assumed for *ctrA* promoters in order to produce a large amount of CtrA (~22,000 molecules, [11]). For the CtrA phosphorylation and degradation, a recently identified CckA→ChpT→CtrA phosphorelay is responsible for the phosphorylation of CtrA and another CckA→ChpT→CpdR phosphorelay inhibits ClpXP protease for CtrA (Fig. 3A), and both pathways are shown to be negatively regulated by DivK~P [12-14], a single domain response regulator whose expression is positively regulated by CtrA~P [15-16]. In the model, a further simplification is made so that the CckA→ChpT→(CtrA, CpdR) pathways remain active until DivK~P reaches a threshold concentration at the later predivisional stage, and then CtrA stops being phosphorylated and is rapidly cleared from the stalk compartment by ClpXP. This assumption is based on the observation that the inner membrane compartmentalization occurring prior to cell division allows fast degradation of CtrA [11] and the inner membrane compartmentalization event is assumed to coincide with the event of DivK~P reaching its threshold.

DivK **:** DivK is present throughout the cell cycle and peaks slightly at the late predivisional cell stage [17-18]. It co-localizes with DivJ kinase at the stalk pole after swarmer to stalk differentiation while its phosphatase, PleC, is localized at the opposite pole [18-20]. The expression of *divK* is directly activated by CtrA~P [15-16] and a relatively large binding constant between CtrA~P and the *divK* promoter is assumed to account for the late activation of *divK* expression [18]. Also, a relatively low *divK* promoter activity is assigned in the model to be in accordance with the measured activity [17]. DivK protein is very stable [18] and we apply a degradation rate to only account for the dilution effect by cell growth. The phosphorylation of DivK is modeled as a pseudo-second-order reaction with the rate depending on the amount of polar localized DivJ and its half-life in the phosphorylation reaction. The transformation of DivK~P to DivK is modeled as a first-order reaction with rate constant determined by the DivK~P half-life in the dephosphorylation reaction. A recent experiment identified another independent *in vivo* pathway for regulating DivK phosphorylation by DivL [21] and this is modeled as the second DivK phosphorylation mechanism, whose first-order rate constant is defined by the half-life of DivK in this pathway. However, more recent experiments have shown that DivL functions as a localization factor that recruits CckA and promotes CtrA phosphorylation [22]. The apparent regulation of DivK phosphorylation by DivL observed in [21] may arise from this newly identified pathway.

Regardless, the specific mechanism that contributes to the minor DivK phosphorylation pathway is not crucial and our model assumes DivL directly or indirectly promotes DivK phosphorylation.

DivJ **:** The activity of the *divJ* promoter peaks during swarmer-stalk transition and DivJ concentration remains relatively constant throughout the rest of cell cycle [19, 23]. This also indicates that DivJ is relatively stable therefore its degradation rate constant is chosen to be the same as DivK. Although direct regulation of the *divJ* promoter has not been identified, we assume that DivJ is very slowly synthesized during the stalk cell cycle to compensate for its degradation under the regulation of CtrA~P. The possibility that CtrA indirectly regulates DivJ [24-25] makes this assumption reasonable. In modeling the DivJ-mediated DivK phosphorylation, a constraint is placed on the number of DivJ proteins that can be adsorbed to the stalked pole and that phosphorylate DivK.

Stochastic Simulation of the Simplified *Caulobacter* Network

To assess the effect of molecular noise on cell cycle oscillation, we simulate the network with the Gillespie method [26], which randomly picks the type of reaction that takes place at every time step as well as the time interval between each step according to the probabilities of individual reactions inside the system. We perform the stochastic simulation by grouping each linear and nonlinear term that appears in the deterministic mode (Table S2) into sequenced reactions and attributing different probabilities to each of these reactions based on the rate constants and number of molecules of all species involved. This is the so-called "non-detailed" stochastic model [27] that does not decompose each nonlinear term into elementary reactions and incorporates quasi-steady-state assumption [28]. Table S5 includes a list of these sequenced reactions (13 reactions) as well as the probability and changes of molecular species for each reaction. To obtain the statistics of the cell cycle oscillation periods as in Figure 4B and Figure S4, each simulation is done with the same initial conditions and the CtrA~P trajectory is used to calculate inter-peak distances that are larger than a preset minimum distance (20 min). To ensure that each simulation is fully independent on the initial conditions, the initial 1000 min of each trajectory (10,000 min) is discarded in calculating the period. The source code (Matlab) is included as a supplement to the manuscript.

Mutant Simulations

For deterministic mutant simulations shown in Figure S2, alternations of parameters as listed in Table S4 are introduced at 200 min following the wild-type simulation for each type of mutant. Trajectories are normalized to the maximum levels of individual species. Most of these are adopted from some of the mutants described in a recent *Caulobacter* model [7] except for the Δ*divJ* mutant. For stochastic simulations with Δ*divJ* without constitutive induction, all parameters are the same as wild-type other than setting $k_{s,divj} = 0$ and the same initial conditions as the wild-type are used except setting cDivJ0 = 0. With xylose induction, DivJ is assumed to be constitutively expressed starting from time zero at a rate of $k_{s,divj}^{*}$ without the control by CtrA~P, i.e. a_{12} in Table S5 becomes $a_{12} = k_{s,divj}^{*} \times \Omega$ and $k_{s,divj}^{*}$ value is described in each figure legend. For simulations in Figure S4A, the DivL-mediated DivK phosphorylation pathway is altered by changing the parameter hlDivKp2 in Table S5 into values as described in the figure legend.

Diffusion-and-Capture Model Simulation for DivJ-EGFP Subcellular Localization

Four species are included in the model described in Figure 7D. "A" represents lateral membrane-bound dark DivJ-EGFP, "A*" represents lateral membrane-bound bright DivJ-EGFP, "AS" represents pole localized dark DivJ-EGFP, and "A*S" represents pole localized bright DivJ-EGFP. The symbol "S" represents the adsorption site on the adsorber. A total of 13 reaction pathways are described in Table S6, including the probability for each pathway and the resulting transitions. Model parameters and initial conditions are included in Table S7.

This model assumes a constant volume of the cell throughout the simulation time course. The dilution effect by cell division is modeled by first-order degradation reaction with half-life similar to the cell cycle time (Table S6). We simulate the temporal trajectories of the numbers of individual species with an exact stochastic approach as described in [26]. Simulations presented are based on the same parameter set except for k_1 as noted in each figure legend. The source code (Matlab) is included as a supplement for the manuscript.

We scale the simulated trajectories of A* and A*S molecule numbers as intensities for direct comparison with experimental trajectories (Figure 7E vs. Figure 7C; Figure S6 vs. Figure S5). We note that the simulation outputs are the number of molecules in a constant cell membrane surface area (or pole surface area); while the experimentally measured intensities are the measures of concentration. The two measures (i.e. total number of molecules and mean fluorescence intensities) are reconciled by the following approach. We first identify the parameter regime of DivJ-EGFP expression rate k_1 that corresponds to our experimental conditions (i.e. different xylose concentrations) with the rest of parameters fixed in the model. The ratio between the number of bright molecules on the lateral membrane over that on the stalked pole, is used to for quantitative comparison between experiment and simulation. Experimentally, we analyze the integrated intensities at the lateral membrane and the stalked pole at the instance when each cell just finished a round of reproduction (and after >6hrs of induction). The ratio between the integrated lateral and stalked intensities is plotted in Figure S7A. We use the data from 0.00015% to 0.015% xylose to construct a linear fit (Figure S7A, red) since the error bar for 0.000015% data is too large. Both the linear trend (including the fitted intercept) and the absolute ratios are in good agreement with those from simulations (compare with the region from $k_1 = 0.02$ to 0.5 in Figure S7B). Therefore, each of our xylose induction concentrations can be mapped to a specific k_1 value in simulation by relating the lateral/stalked ratio with the A*/A*S ratio. With this mapping and with the simulated trajectory with each mapped k_1, we scale the number of molecules in the trajectory to the measurement intensity (as in Figure 7C) according to the quantified steady-state intensities for the corresponding experimental induction concentration (i.e. Figure 7F). For the experimental trajectory shown in Figure 7C (0.015% xylose), its simulation counterpart is shown in Figure 7E ($k_1 = 0.37$). And for other conditions, the experiments are also mapped to their simulation counterparts (Figure S5 and Figure S6), specifically the mapped k_1 parameter values for 0.0015%, 0.00015%, and 0.000015% xylose are 0.28, 0.20, and 0.11, respectively.

Supplementary Figures

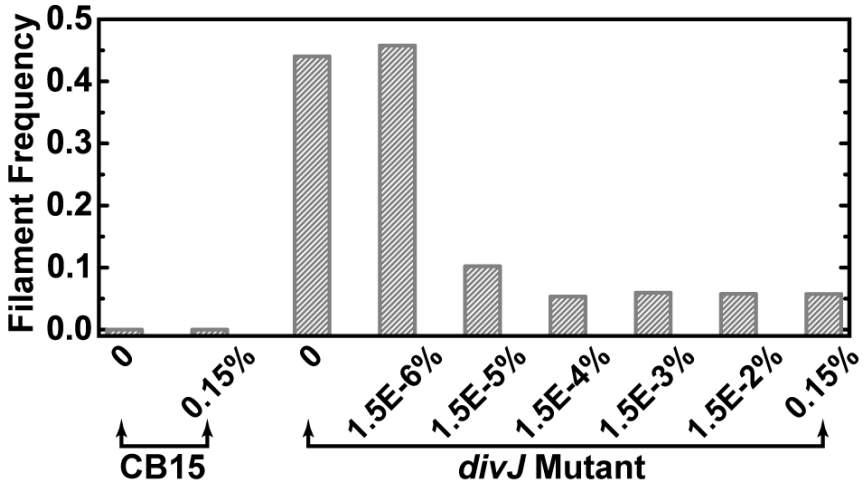

Figure S1. Single-cell analysis of morphological defects in the *divJ* mutant for different xylose induction levels.

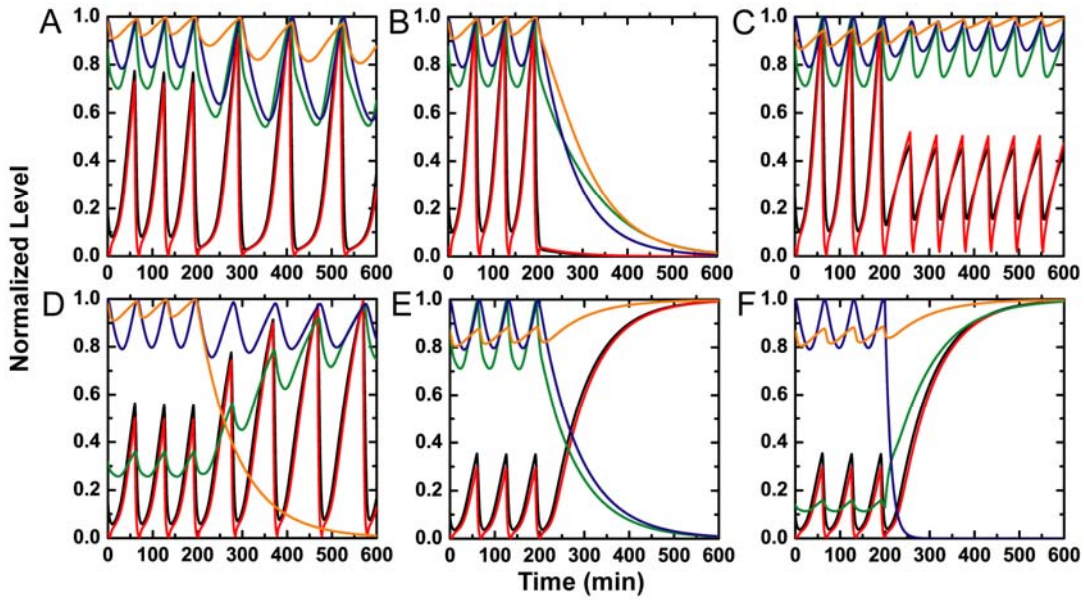

Figure S2. Mutant simulations for cell cycle model by deterministic method. (A) Δ*ctrA P1*, (B) Δ*ctrA*, (C) Δ*ctrA*+P_{xyl}-*ctra*, (D) Δ*divJ*, (E) Δ*divK*, and (F) DivK phosphorylation defect mutant $DivK_{D53A}$. Mutations are introduced at t = 200 min by altering the corresponding parameters. Parameter changes and explanations are summarized in Table S4. The color scheme is the same as Figure 3.

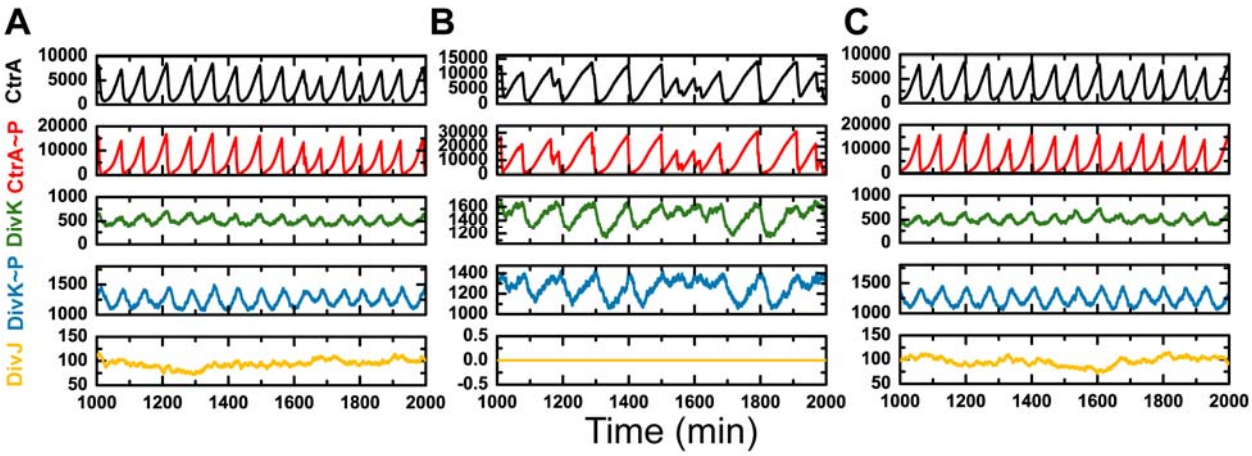

Figure S3. Representative trajectories from stochastic simulations of the simplified cell cycle model. (A) Wild-type trajectories. (B) Δ*divJ* mutant trajectories ($k_{s,divj}$ = 0, cDivJ0=0). (C) Constitutive induction of *divJ* for Δ*divJ* mutant ($k_{s,divj}^{*}$ = 0.04 nM/sec). Refer to Supplementary Methods for details of wild-type and mutant stochastic simulations.

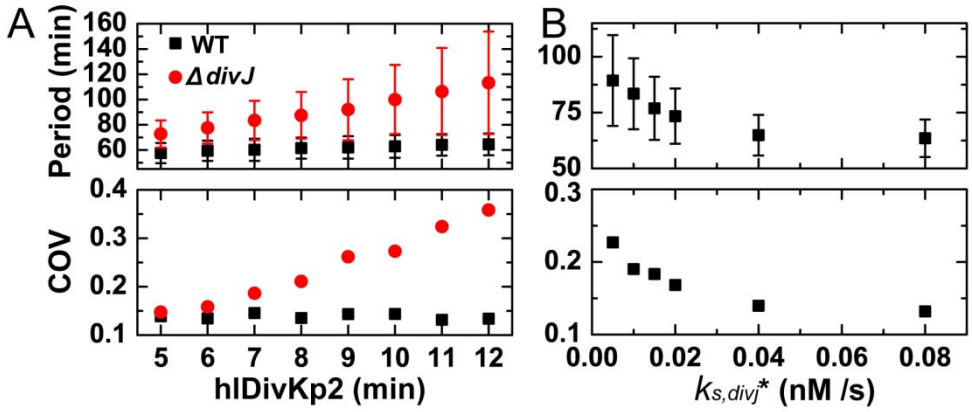

Figure S4. Simulated CtrA~P oscillation period statistics. (A) CtrA~P oscillation period statistics for different strengths of the DivL-mediated DivK phosphorylation pathway. Wild-type and Δ*divJ* mutant simulations are done as described in the Supplementary Methods. All parameters are kept the same except that the parameter hlDivKp2 (min) is varied as indicated in the horizontal axis. Note that we adopt hlDivKp2 = 10 min (Table S3) for all other simulations presented in the paper. (B) CtrA~P oscillation period statistics under different DivJ induction rates ($k_{s,divj}^{*}$) for Δ*divJ* mutant. $k_{s,divj}^{*}$ is varied from 0.005 to 0.08 nM/sec.

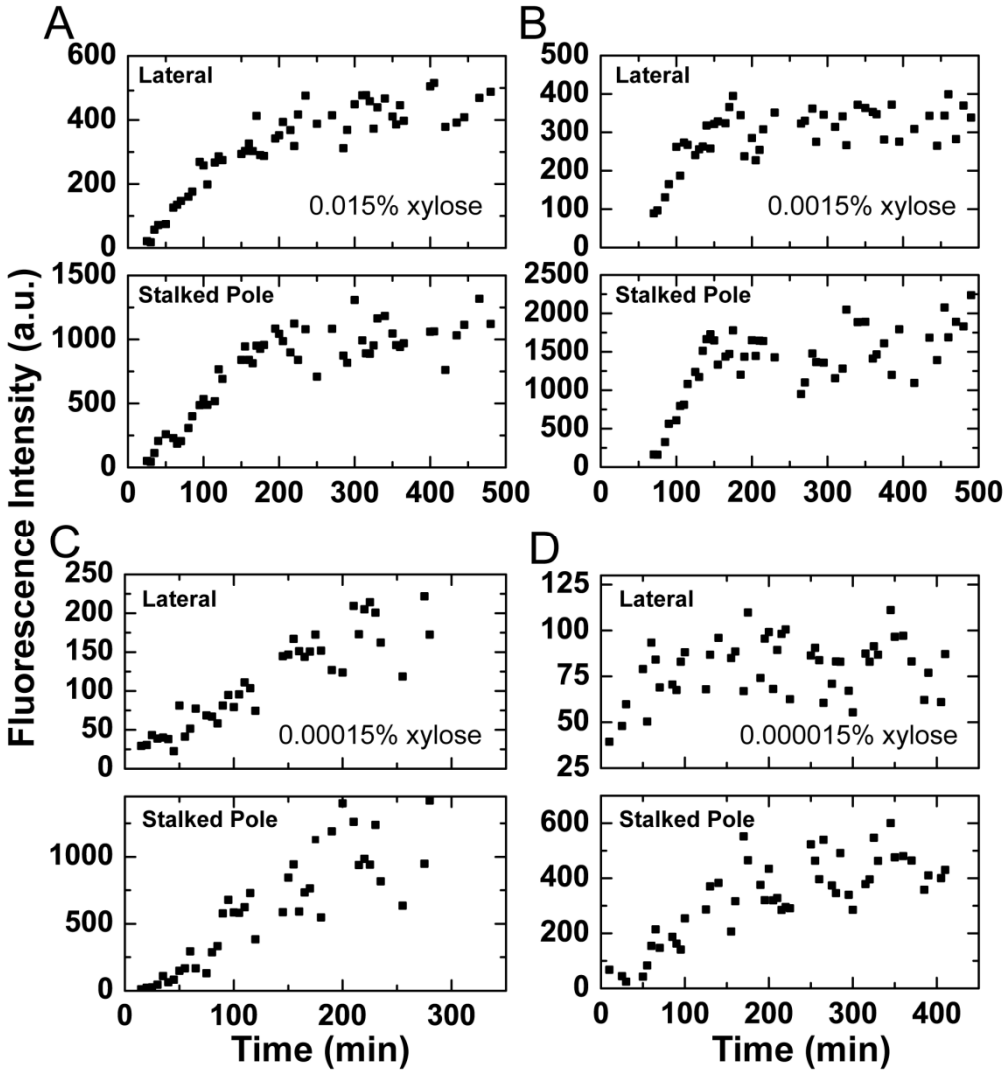

Figure S5. Experimental single-cell fluorescence intensity traces. Example single *C. crescentus* cell lateral membrane and stalked pole temporal intensity trajectories for different xylose induction levels are shown: 0.015% xylose (A), 0.0015% xylose (B), 0.00015% xylose (C), and 0.000015% xylose (D). Note that panel (A) is a replica of Figure 7C.

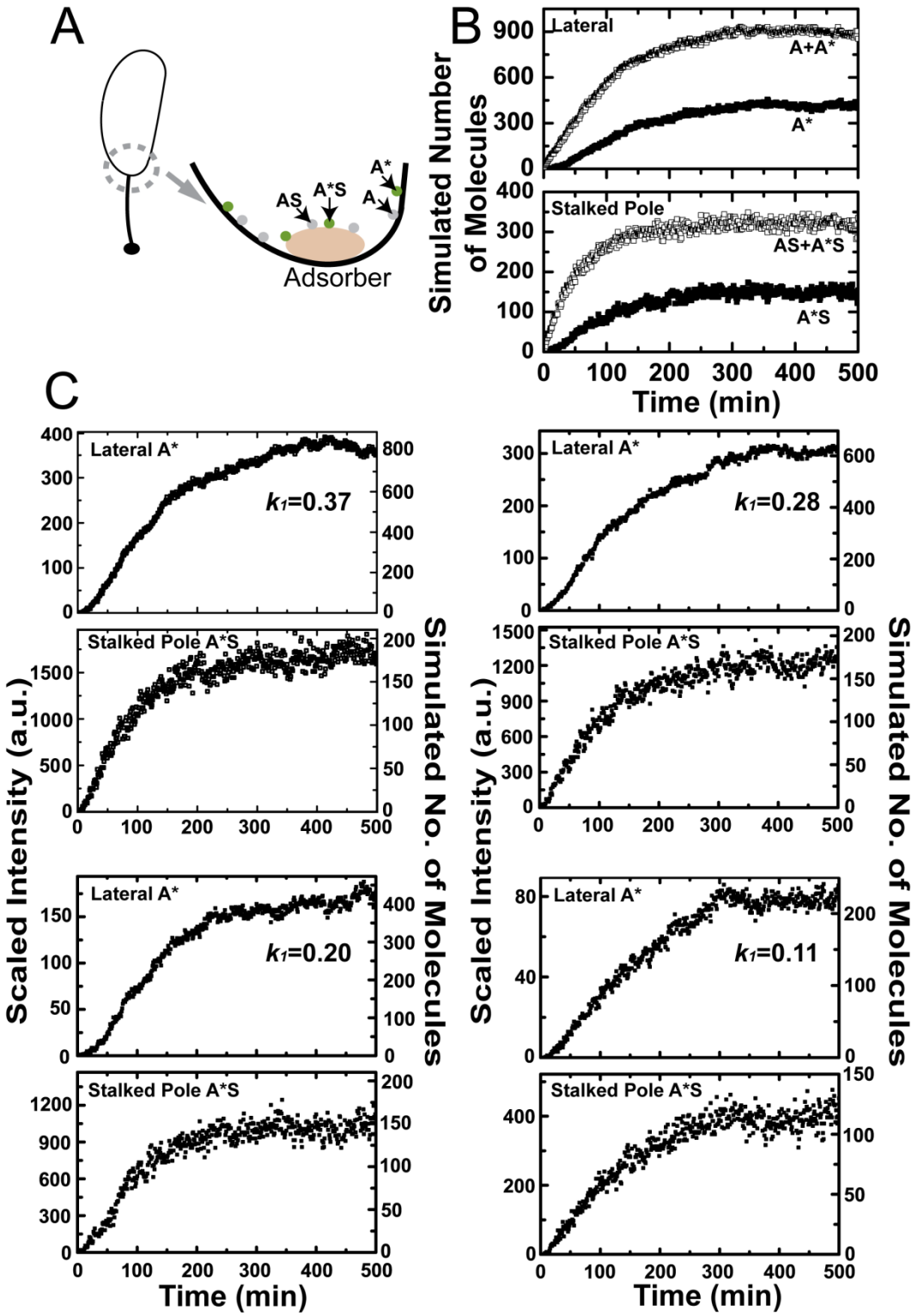

Figure S6. Model simulation for DivJ-EGFP kinetics. (A) Cartoon illustration of the simulated species. (B) Example simulated time traces for different species as indicated at k_1 = 0.2. (C) Example simulated temporal traces for A* and A*S for different production rates as indicated. Each k_1 corresponds to an experimental induction condition (See Supplementary Methods). The intensity scale (for comparison with experimental trajectories) is shown on the left Y-axis while the scale for the number of molecules (simulation output) is shown on the right. Note that k_1 = 0.37 panel is a replica of Figure 7E.

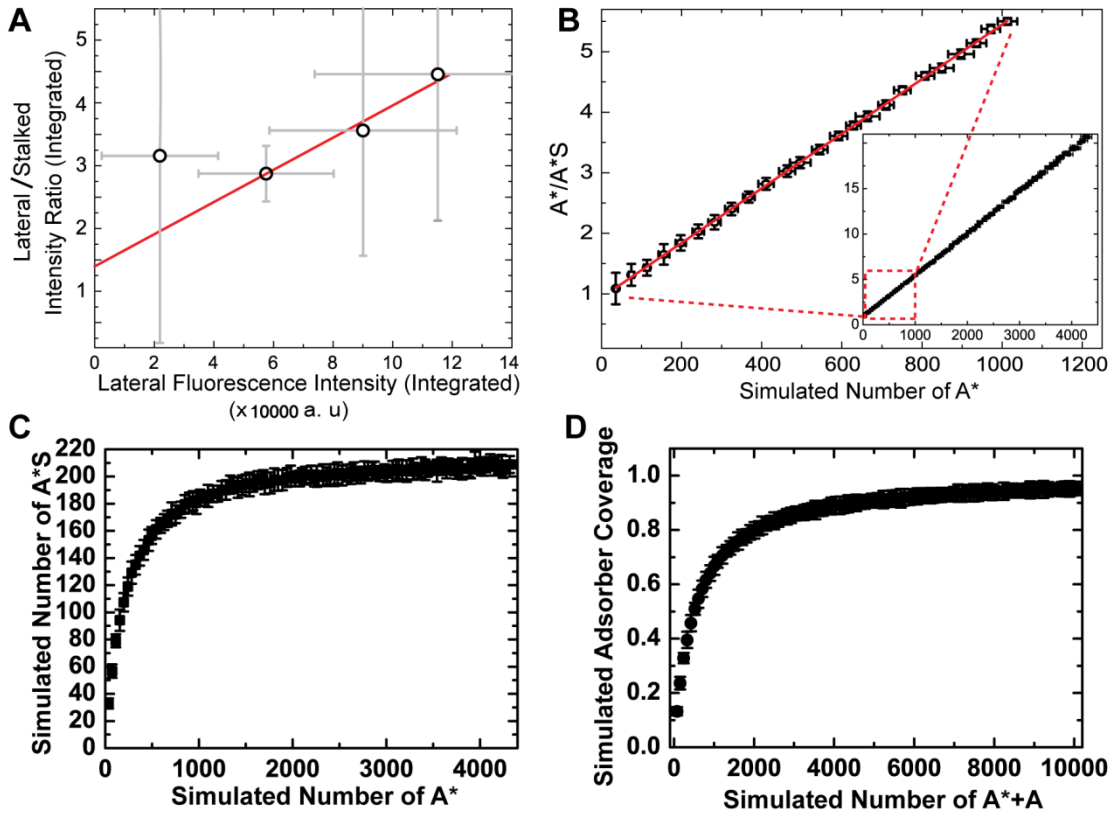

Figure S7. Experimental and simulated DivJ-EGFP steady states, and the simulated adsorption/desorption isotherm. (A) Ratio of the integrated lateral membrane fluorescence over the integrated stalked pole fluorescence at steady states under different xylose levels. Red line is a linear fit of the rightmost three data points ($y=2.57*10^{-5}x+1.39$). See Supplementary Methods for details. (B) Simulation counterpart of (A). The ratio A*/A*S is plotted against the number of A* from simulations with $k_1 = 0.02$ to 0.5. The line fit (solid red) gives $y=0.00451x+0.940$. The insert shows the same plot for a larger range of k_1, i.e. from 0.02 to 2. (C) Simulated steady states levels of A* and A*S from $k_1 = 0.02$ to 2. These levels are used for construction of (B). (D) Simulated adsorption/desorption isotherm from $k_1 = 0.02$ to 2. The adsorber coverage (number of AS+A*S over number of total adsorber sites) is plotted against the number of bath protein molecules (A+A*).

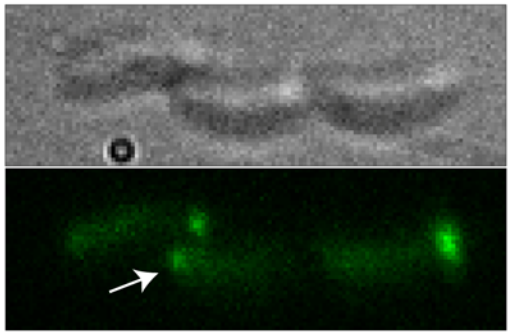

Figure S8. Premature localization of DivJ-EGFP to the flagellated pole in a late predivisional cell (lower cell). Shown are *C. crescentus* cells in microfluidic culture expressing DivJ-EGFP (*divJ*::Tn5 cells expressing *divJ-egfp* from the *xylX* chromosomal locus) under 0.015% xylose induction. Bright-field DIC image (top) and a false-color fluorescence image from the same area (bottom). The flow direction is from right to left.

Supplementary Tables

Table S1. Summary of measured single-cell division times. This table corresponds to Figure 2B.

Strain	Xylose (w/v)	ST Cell Cycle (Mean ± SD, min)	COV (SD/Mean)	Number of ST Cycle N_{ST}	SW Cell Cycle (Mean ± SD, min)	COV (SD/Mean)	Number of SW Cycle N_{SW}
CB15	0	60.6 ± 7.6	0.125	519	75.0 ± 7.5	0.100	118
	0.15%	61.6 ± 7.5	0.122	444	76.3 ± 7.8	0.102	92
CB15 *divJ*::Tn5 + pMR20 -P_{xyl}-*divJ*	0	76.2 ± 18.7	0.246	224	92.2 ± 26.2	0.284	71
	1.5×10^{-6} %	72.0 ± 12.3	0.171	195	86.3 ± 18.4	0.213	57
	1.5×10^{-5} %	66.8 ± 8.9	0.134	387	77.0 ± 8.3	0.108	97
	1.5×10^{-4} %	67.1 ± 8.4	0.125	253	75.2 ± 7.6	0.101	59
	1.5×10^{-3} %	67.5 ± 9.0	0.134	689	75.8 ± 10.1	0.133	49
	1.5×10^{-2} %	65.4 ± 7.9	0.121	412	74.0 ± 8.5	0.115	41
	0.15%	67.2 ± 10.3	0.154	649	72.5 ± 7.7	0.106	56

Table S2. Differential equations for cell cycle oscillation model described in Figure 3A.

$\frac{d[\text{CtrA}]}{dt} = k_{s1,ctra}\frac{K_{d1,\text{CtrA}-\text{CtrA}}^{n}}{K_{d1,\text{CtrA}-\text{CtrA}}^{n}+[\text{CtrA}\sim\text{P}]^{n}} + k_{s2,ctra}\frac{[\text{CtrA}\sim\text{P}]^{n}}{K_{d2,\text{CtrA}-\text{CtrA}}^{n}+[\text{CtrA}\sim\text{P}]^{n}} + k_{dp,ctrap}[\text{CtrA}\sim\text{P}]$ $-(k_{p1,ctra}\cdot\text{phosphosignal}+k_{p2,ctra})[\text{CtrA}]-\left(k_{d1,ctra}\cdot\text{clpXP}+k_{d2,ctra}\right)\ [\text{CtrA}]$
$\frac{d[\text{CtrA}\sim\text{P}]}{dt} = (k_{p1,ctra}\cdot\text{phosphosignal}+k_{p2,ctra})[\text{CtrA}]-k_{dp,ctrap}[\text{CtrA}\sim\text{P}]$ $-\left(k_{d1,ctra}\cdot\text{clpXP}+k_{d2,ctra}\right)\ [\text{CtrA}\sim\text{P}]$
$\frac{d[\text{DivK}]}{dt} = k_{s,divk}\frac{[\text{CtrA}\sim\text{P}]^{n}}{K_{d,\text{CtrA}-\text{DivK}}^{n}+[\text{CtrA}\sim\text{P}]^{n}} + k_{dp,divkp}[\text{DivK}\sim\text{P}]$ $-(k_{p1,divk}\lambda_{DivJ}+k_{p2,divk})[\text{DivK}]-k_{d,divk}[\text{DivK}]$
$\frac{d[\text{DivK}\sim\text{P}]}{dt} = (k_{p1,divk}\lambda_{DivJ}+k_{p2,divk})[\text{DivK}]-k_{dp,divkp}[\text{DivK}\sim\text{P}]-k_{d,divk}[\text{DivK}\sim\text{P}]$
$\frac{d[\text{DivJ}]}{dt} = k_{s,divj}\frac{[\text{CtrA}\sim\text{P}]^{n}}{K_{d,\text{CtrA}-\text{DivJ}}^{n}+[\text{CtrA}\sim\text{P}]^{n}} - k_{d,divj}[\text{DivJ}]$
When $[\text{DivK}\sim\text{P}]\geq[\text{DivKP}]_{\text{TH}}$, phosphosignal = 0 and clpXP = 1; otherwise, phosphosignal = 1 and clpXP = 0. λ_{DivJ} is defined as $\min\left\{\frac{[\text{DivJ}]}{[\text{DivJ}]_{\text{TH}}},\ 1\right\}$.

Table S3. Parameters and initial conditions for cell cycle model described in Figure 3A and Table S2.

Symbol	Parameter	Value (unit)	Related Parameter (unit)	Source / Note
hlCtrAd1	Half-life for CtrA (and CtrA~P) degradation with ClpXP	2 (min)	$k_{d1,ctra} = \frac{\ln(2)}{60 \times \text{hlCtrAd1}}$ (s^{-1})	The half-life of CtrA is less than 5 min [29].
hlCtrAd2	Half-life for CtrA (and CtrA~P) degradation without ClpXP	52 (min)	$k_{d2,ctra} = \frac{\ln(2)}{60 \times \text{hlCtrAd2}}$ (s^{-1})	[30].
hlCtrAp1	Half-life for CtrA phosphorylation with phosphosignal	2 (min)	$k_{p1,ctra} = \frac{\ln(2)}{60 \times \text{hlCtrAp1}}$ (s^{-1})	The cell cycle profile of CtrA~P follows that of CtrA [29], indicating the fast phosphorylation of CtrA.
hlCtrAp2	Half-life for CtrA phosphorylation without phosphosignal	100 (min)	$k_{p2,ctra} = \frac{\ln(2)}{60 \times \text{hlCtrAp2}}$ (s^{-1})	CtrA is barely phosphorylated without phosphosignal from active CckA [31].
hlCtrAPdp	Half-life for CtrA~P dephosphorylation	5 (min)	$k_{dp,ctrap} = \frac{\ln(2)}{60 \times \text{hlCtrAPdp}}$ (s^{-1})	The half-life of CtrA~P is less than 5min, which may due to both degradation and dephosphorylation [29].
hlDivKd	Half-life for DivK (and DivK~P) degradation	60 (min)	$k_{d,divk} = \frac{\ln(2)}{60 \times \text{hlDivKd}}$ (s^{-1})	No significant degradation of DivK over long time course [6, 18]. 60 min is taken to account for the dilution due to doubling in volume every cycle.
hlDivKp1	Half-life for DivK phosphorylation through DivJ	5 (min)	$k_{p1,divk} = \frac{\ln(2)}{60 \times \text{hlDivKp1}}$ (s^{-1})	[17]
hlDivKp2	Half-life for DivK phosphorylation through DivL	10 (min)	$k_{p2,divk} = \frac{\ln(2)}{60 \times \text{hlDivKp2}}$ (s^{-1})	DivL pathway is estimated to be ~one fold slower than DivJ from [21].
hlDivKPdp	Half-life for DivK~P dephosphorylation	10 (min)	$k_{dp,divkp} = \frac{\ln(2)}{60 \times \text{hlDivKPdp}}$ (s^{-1})	The phosphatase PleC only transiently localizes to the stalk pole in the stalk cell [19], therefore we use the dephosphorylation rate in the absence of PleC. This time

				constant is estimated from [25].
hlDivJd	Half-life for DivJ degradation	60 (min)	$k_{d,divj} = \frac{\ln(2)}{60 \times \text{hlDivJd}}$ (s^{-1})	The *divJ* promoter activity peaks at swarmer to stalk transition [23], and the DivJ level stays almost constant through the rest of cell cycle [19]. We therefore assume that DivJ is relatively stable.
$k_{s1,ctra}$	Maximum rate for CtrA production from *ctrA* P1 promoter.	10 (nM/s)	About 22,000 CtrA molecules [11] are present in the late predivisional cell and this rate is chosen to account for such fast synthesis of CtrA.	
$k_{s2,ctra}$	Maximum rate for CtrA production from *ctrA* P2 promoter.	35 (nM/s)	*ctrA* P2 promoter is stronger than *ctrA* P1 promoter [8-9]). It is estimated that P2 promoter is ~ 3 times as strong as P1 promoter [3].	
$k_{s,divk}$	Maximum rate for DivK production from *divK* promoter.	1.6 (nM/s)	According to study of protein synthesis along cell cycle progression [6], we estimated the number of DivK proteins in predivisional cell to be ~ 10% of CtrA, i.e. about 2000 molecules. Accordingly, we choose a relatively low DivK synthesis rate.	
$k_{s,divj}$	Maximum rate for DivJ production from *divJ* promoter.	0.05 (nM/s)	Most of DivJ is synthesized during swarmer to stalk transition [23] and there is only little variation in DivJ level after the transition [19] , so we assume a very low synthesis rate.	
$K_{d1,CtrA\text{-}CtrA}$	Binding constant between CtrA~P and *ctrA* P1 promoter site.	1,500 (nM)	CtrA~P inhibits *ctrA* P1 and transcripts from *ctrA* P1 peaks in the early stalk cell [8]. This constant is chosen so that the expression of *ctrA* P1is barely inhibited until CtrA~P concentration exceeds 1500nM, i.e. roughly in the early stalked cell.	
$K_{d2,CtrA\text{-}CtrA}$	Binding constant between CtrA~P and *ctrA* P2 promoter site.	9,000 (nM)	CtrA~P activates *ctrA* P2 and transcripts from *ctrA* P2 peaks in the late predivisional cell [8]. This constant is chosen so that the expression of *ctrA* P2 is fully activated until CtrA~P concentration exceeds 9000 nM.	
$K_{d,CtrA\text{-}DivK}$	Binding constant between CtrA~P and *divK* promoter site.	9,000 (nM)	CtrA~P directly activates DivK expression [15-16]. DivK is present through the cell cycle and peaks at the late predivisional cell [17-18]. This constant is chosen so that the expression of *divK* is fully activated until CtrA~P concentration exceeds 9000 nM..	
$K_{d,CtrA\text{-}DivJ}$	Binding constant between CtrA~P and *divJ* promoter site.	1,500 (nM)	Although it has not been shown that CtrA~P directly activates the expression of *divJ*, there are evidences indicating that CtrA~P might indirectly regulate DivJ [24-25]. We therefore assume CtrA~P promotes the synthesis of DivJ in the model.	
$[\text{DivKP}]_{TH}$	Threshold DivK concentration to induce the loss of phosphosignal and trigger fast CtrA	3000 (nM)	The accumulation of DivK~P in the late predivisional cell inhibits CckA-ChpT-CtrA phosphorelay and also triggers the proteolysis of CtrA [12-13]. We therefore assume that both events will occur when DivK~P concentration exceeds this threshold. This threshold is chosen to match the estimations that there are a maximum of	

	degradation		22,000 CtrA molecules at the late predivisional stage [11].
$[DivJ]_{TH}$	Maximum concentration/number of DivJ that could participate in the phosphorylation of DivK	220 (nM) or 100 (molecules)	This constraint is necessary in modeling our experiment with constitutive expression of *divJ*. We estimated the number of histidine kinase DivJ that localize to the pole in wild-type *Caulobacter* to be on the order of ~100 based on two measurements: a) quantitative Western blot measurement on a typical bacterial two-component system [32]; b) *in vivo* single-molecule fluorescent measurements of another histidine kinase PleC-EYFP in *Caulobacter* [33].
n	Hill coefficient	2	We use $n = 2$ as the Hill coefficient.
cCtrA0	Initial concentration of CtrA	4600 (nM)	This concentration corresponds 13% of its peak level in wild-type.
cCtrAP0	Initial concentration of CtrA~P	1250 (nM)	This concentration corresponds to ~570 CtrA~P molecules and is 2% of its peak level in wild-type. Low CtrA~P is necessary otherwise DNA replication is inhibited [34].
cDivK0	Initial concentration of DivK	1150 (nM)	DivK presents throughout the cell cycle and only increases slightly in later cell cycle stage [18].
cDivKP0	Initial concentration of DivK~P	3100 (nM)	DivK~P level stays almost constant after swarmer to stalk transition [18].
cDivJ0	Initial concentration of DivJ	225 (nM)	DivJ level stays almost constant after swarmer to stalk transition [19].

Table S4. Descriptions, changes of parameters, and explanations for *in silico* mutant simulations corresponding to Figure S2.

Mutant Genotype	Description / Reference	Parameter Change	Explanations
Δ*ctrA* P1	Expression from *ctrA* P1 is greatly repressed [9].	$k_{s1,ctra}$ = 1.5 (15% of wild-type [7])	The cells are able to divide but with prolonged division time [9]. Our simulation (Figure S2A) confirms this observation.
Δ*ctrA*	Δ*ctrA::spec ctrA*-null mutant [35].	$k_{s1,ctra}$ = 0; $k_{s2,ctra}$ = 0.	Cell division is arrested [35] and is confirmed by simulation (Figure S2B).
Δ*ctrA* +P_{xyl}-*ctra*	Δ*ctrA::spec* + P_{xyl}-*ctra* [35].	$k_{s1,ctra}$ = 0; $k_{s2,ctra}$ = 0; $k_{pxyl\text{-}ctra}$ = 10.	Cell is viable with the expression of xylose-inducible *ctrA*. [35]. Our simulation (Figure S2C) confirms this observation.
Δ*divJ*	*divJ*-null mutant [19].	$k_{s,divj}$ = 0.	Mutant cells are still able to division but with prolonged division time as shown in our experiment and simulation (Figure S2D).
Δ*divK*	*divK*-null mutant [17].	$k_{s,divk}$ = 0.	DivK is essential to the cell [17] and our simulation shows the division is arrested (Figure S2E).
$DivK_{D53A}$	Suppression of DivK phosphorylation with mutated amino acid [20].	$k_{p1,divk}$ = 0; $k_{p2,divk}$ = 0.	DivK phosphorylation is essential to the cell [20] and our simulation shows the division is arrested (Figure S2F).

Table S5. Stochastic simulation for the cell cycle model described in Figure 3A and Table S2.

#	Reaction	Description	Probability	Transitions
1	→ CtrA	Production of CtrA	$a_1 = (k_{s1,ctra}\Omega)\frac{(K_{d1,\mathrm{CtrA-CtrA}}\Omega)^n}{(K_{d1,\mathrm{CtrA-CtrA}}\Omega)^n + \mathrm{CtrA{\sim}P}^n} + (k_{s2,ctra}\Omega)\frac{\mathrm{CtrA{\sim}P}^n}{(K_{d2,\mathrm{CtrA-CtrA}}\Omega)^n + \mathrm{CtrA{\sim}P}^n}$	CtrA → CtrA+1
2	CtrA → CtrA~P	Phosphorylation of CtrA	$a_2 = (k_{p1,ctra} \cdot \mathrm{phosphosignal} + k_{p2,ctra}) \times \mathrm{CtrA}$	CtrA → CtrA-1 CtrA~P → CtrA~P+1
3	CtrA~P → CtrA	Dephosphorylation of CtrA~P	$a_3 = k_{dp,ctrap} \times \mathrm{CtrA{\sim}P}$	CtrA → CtrA+1 CtrA~P → CtrA~P-1
4	CtrA → Ø	Degradation of CtrA	$a_4 = \left(k_{d1,ctra} \cdot \mathrm{clpXP} + k_{d2,ctra}\right) \times \mathrm{CtrA}$	CtrA → CtrA-1
5	CtrA~P → Ø	Degradation of CtrA~P	$a_5 = \left(k_{d1,ctra} \cdot \mathrm{clpXP} + k_{d2,ctra}\right) \times \mathrm{CtrA{\sim}P}$	CtrA~P → CtrA~P-1
6	→ DivK	Production of DivK	$a_6 = (k_{s,divk}\Omega)\frac{\mathrm{CtrA{\sim}P}^n}{(K_{d,\mathrm{CtrA-DivK}}\Omega)^n + \mathrm{CtrA{\sim}P}^n}$	DivK → DivK+1
7	DivK → DivK~P (by DivJ)	Phosphorylation of DivK through DivJ pathway	$a_7 = k_{p1,divk}\lambda_{DivJ} \times \mathrm{DivK}$	DivK → DivK-1 DivK~P → DivK~P+1
8	DivK → DivK~P (by DivL)	Phosphorylation of DivK through DivL pathway	$a_8 = k_{p2,divk} \times \mathrm{DivK}$	DivK → DivK-1 DivK~P → DivK~P+1
9	DivK~P → DivK	Dephosphorylation of DivK~P	$a_9 = k_{dp,divkp} \times \mathrm{DivK{\sim}P}$	DivK → DivK+1 DivK~P → DivK~P-1
10	DivK → Ø	Degradation of DivK	$a_{10} = k_{d,divk} \times \mathrm{DivK}$	DivK → DivK-1
11	DivK~P → Ø	Degradation of DivK~P	$a_{11} = k_{d,divk} \times \mathrm{DivK{\sim}P}$	DivK~P → DivK~P-1
12	→ DivJ	Production of DivJ	$a_{12} = (k_{s,divj}\Omega)\frac{\mathrm{CtrA{\sim}P}^n}{(K_{d,\mathrm{CtrA-DivJ}}\Omega)^n + \mathrm{CtrA{\sim}P}^n}$	DivJ → DivJ+1
13	DivJ → Ø	Degradation of DivJ	$a_{13} = k_{d,divj} \times \mathrm{DivJ}$	DivJ → DivJ-1

Ω is conversion constant from nM to number of molecules, i.e. $\Omega = \frac{1\ \mathrm{nM}}{2.2\ \mathrm{nM/per\ molecule}}$ (6).

All species are described in number of molecules and are converted, i.e. $\mathrm{DivJ} = [\mathrm{DivJ}] \times \Omega$.

Thresholds ($\mathrm{DivJ_{TH}}$ and $\mathrm{DivK_{TH}}$) are also in number of molecules.

Table S6. Modeling of DivJ-EGFP dynamics described in Figure 7D, including 13 reaction pathways and their probabilities and corresponding transitions.

Reaction #	Reaction	Description	Probability	Transitions
1	$\rightarrow$ A	Production of DivJ-EGFP	$a_1 = k_1$	$A \rightarrow A+1$
2	A $\rightarrow$ A*	Chromophore maturation of membrane bound DivJ-EGFP	$a_2 = k_4 \times A$	$A \rightarrow A-1$ $A^* \rightarrow A^*+1$
3	A* $\rightarrow$ A	Chromophore unfolding of membrane bound DivJ-EGFP	$a_3 = k_5 \times A^*$	$A \rightarrow A+1$ $A^* \rightarrow A^*-1$
4	A $\rightarrow$ Ø	Degradation of membrane bound dark DivJ-EGFP	$a_4 = k_{da} \times A$	$A \rightarrow A-1$
5	A* $\rightarrow$ Ø	Degradation of membrane bound bright DivJ-EGFP	$a_5 = k_{da} \times A^*$	$A^* \rightarrow A^*-1$
6	A +S $\rightarrow$ AS	Polar adsorption of membrane bound dark DivJ-EGFP	$a_6 = k_2 \times A \times S$	$A \rightarrow A-1$ $AS \rightarrow AS+1$ $S \rightarrow S-1$
7	AS $\rightarrow$ A+S	Desorption of polar localized dark DivJ-EGFP	$a_7 = k_3 \times AS$	$A \rightarrow A+1$ $AS \rightarrow AS-1$ $S \rightarrow S+1$
8	A* +S $\rightarrow$ A*S	Polar adsorption of membrane bound bright DivJ-EGFP	$a_8 = k_2 \times A^* \times S$	$A^* \rightarrow A^*-1$ $A^*S \rightarrow A^*S+1$ $S \rightarrow S-1$
9	A*S $\rightarrow$ A*+S	Desorption of polar localized bright DivJ-EGFP	$a_9 = k_3 \times A^*S$	$A^* \rightarrow A^*+1$ $A^*S \rightarrow A^*S-1$ $S \rightarrow S+1$
10	AS $\rightarrow$ A*S	Chromophore maturation of pole localized DivJ-EGFP	$a_{10} = k_4 \times AS$	$AS \rightarrow AS-1$ $A^*S \rightarrow A^*S+1$
11	A*S $\rightarrow$ AS	Chromophore unfolding of pole localized DivJ-EGFP	$a_{11} = k_5 \times A^*S$	$AS \rightarrow AS+1$ $A^*S \rightarrow A^*S-1$
12	AS $\rightarrow$ Ø	Degradation of pole localized dark DivJ-EGFP	$a_{12} = k_{das} \times AS$	$AS \rightarrow AS-1$ $S \rightarrow S+1$
13	A*S $\rightarrow$ Ø	Degradation of pole localized bright DivJ-EGFP	$a_{13} = k_{das} \times A^*S$	$A^*S \rightarrow A^*S-1$ $S \rightarrow S+1$

Table S7. Parameters and initial conditions for the DivJ-EGFP model described in Figure 7D and Table S6.

Symbol	Parameter	Value (unit)	Source / Note
k_1	Production rate of DivJ-EGFP	0.37 (s^{-1})	This rate is $0.37s^{-1}$ in Fig. 7E, and is varied in Figs. S6 and S7 as indicated.
k_2	Second-order rate constant for adsorption of membrane bound DivJ-EGFP	2.31×10^{-5} (s^{-1})	Assuming a pseudo-first-order kinetics at the beginning of the reaction (i.e. adsorber site S assumed to be a constant as 500), $k_2 \times S$ yields a 60 sec half-life for polar adsorption of membrane bound protein, which is comparable to the diffusion time of membrane protein across whole cell body [36].
k_3	First-order rate constant for desorption of pole localized DivJ-EGFP	0.0116 (s^{-1})	This rate constant yields 60 sec half-life for desorption of pole localized protein. This constant is chosen according to k_2 and our experimental traces.
k_4	First-order maturation rate constant of DivJ-EGFP	1.93×10^{-4} (s^{-1})	This rate constant yields 60 min half-life for EGFP maturation. This number is estimated from multiple reported values [37-40].
k_5	First-order unfolding rate constant of DivJ-EGFP	6.42×10^{-5} (s^{-1})	EGFP is known to be stable and this rate constant assumes 3 hrs half-life. We assume minimum photobleaching during our experiment due to relatively low laser power and slow frame rate (1 per 5 min).
k_{da}	First-order degradation rate constant for membrane bound DivJ-EGFP.	1.93×10^{-4} (s^{-1})	This rate constant yields 60 min half-life for membrane bound DivJ-EGFP degradation. This time is assumed to be approximately the cell cycle time in order to account for dilution by cell volume doubling every cell cycle.
k_{das}	First-order degradation rate constant for pole localized DivJ-EGFP.	6.42×10^{-5} (s^{-1})	This rate constant yields 3hrs half-life. Due to adsorption/desorption and fast membrane bound protein degradation, this constant is not critical.
A_0	Initial number of membrane bound dark DivJ-EGFP	0	No A present initially.
A^*_0	Initial number of membrane bound bright DivJ-EGFP	0	No A* present initially.
AS_0	Initial number of pole localized dark DivJ-EGFP	0	No AS present initially.
A^*S_0	Initial number of pole localized bright DivJ-EGFP	0	No A*S present initially.
S_0	Initial number of adsorber sites (i.e. adsorber capacity)	500	This number is chosen by the estimation that the number pole localized DivJ protein is in the order of hundreds (see Table S3).

Source Codes for Models

The source codes for the models (i.e. the deterministic cell cycle model and its stochastic version, and the DivJ-EGFP localization model) described in this manuscript can be downloaded from the *Mol. Syst. Biol.* website.

References for Supplementary Information

1. Yap, P.T. and P. Raveendran, *Image focus measure based on Chebyshev moments*. IEE Proc Vis Image Signal Process, 2004. **151**(2): p. 128-136.
2. Siegal-Gaskins, D. and S. Crosson, *Tightly regulated and heritable division control in single bacterial cells.* Biophys J, 2008. **95**(4): p. 2063-72.
3. Shen, X., et al., *Architecture and inherent robustness of a bacterial cell-cycle control system.* Proc Natl Acad Sci U S A, 2008. **105**(32): p. 11340-5.
4. Brazhnik, P. and J.J. Tyson, *Cell cycle control in bacteria and yeast: a case of convergent evolution?* Cell Cycle, 2006. **5**(5): p. 522-9.
5. Laub, M.T., et al., *Global analysis of the genetic network controlling a bacterial cell cycle.* Science, 2000. **290**(5499): p. 2144-2148.
6. Grunenfelder, B., et al., *Proteomic analysis of the bacterial cell cycle.* Proc Natl Acad Sci U S A, 2001. **98**(8): p. 4681-4686.
7. Li, S., et al., *A quantitative study of the division cycle of Caulobacter crescentus stalked cells.* PLoS Comput Biol, 2008. **4**(1): p. e9.
8. Domian, I.J., A. Reisenauer, and L. Shapiro, *Feedback control of a master bacterial cell-cycle regulator.* Proc Natl Acad Sci U S A, 1999. **96**(12): p. 6648-6653.
9. Reisenauer, A. and L. Shapiro, *DNA methylation affects the cell cycle transcription of the CtrA global regulator in Caulobacter.* EMBO J, 2002. **21**(18): p. 4969-77.
10. Holtzendorff, J., et al., *Oscillating global regulators control the genetic circuit driving a bacterial cell cycle.* Science, 2004. **304**(5673): p. 983-987.
11. Judd, E.M., et al., *Fluorescence bleaching reveals asymmetric compartment formation prior to cell division in Caulobacter.* Proc Natl Acad Sci U S A, 2003. **100**(14): p. 8235-8240.
12. Biondi, E.G., et al., *Regulation of the bacterial cell cycle by an integrated genetic circuit.* Nature, 2006. **444**(7121): p. 899-904.
13. Laub, M.T., L. Shapiro, and H.H. McAdams, *Systems biology of Caulobacter.* Annu Rev Genet, 2007. **41**: p. 429-41.
14. Iniesta, A.A. and L. Shapiro, *A bacterial control circuit integrates polar localization and proteolysis of key regulatory proteins with a phospho-signaling cascade.* Proc Natl Acad Sci U S A, 2008. **105**(43): p. 16602-7.
15. Laub, M.T., et al., *Genes directly controlled by CtrA, a master regulator of the Caulobacter cell cycle.* Proc Natl Acad Sci U S A, 2002. **99**(7): p. 4632-4637.
16. Hung, D.Y. and L. Shapiro, *A signal transduction protein cues proteolytic events critical to Caulobacter cell cycle progression.* Proc Natl Acad Sci U S A, 2002. **99**(20): p. 13160-13165.
17. Hecht, G.B., et al., *An essential single domain response regulator required for normal cell division and differentiation in Caulobacter crescentus.* EMBO J, 1995. **14**(16): p. 3915-24.
18. Jacobs, C., D. Hung, and L. Shapiro, *Dynamic localization of a cytoplasmic signal transduction response regulator controls morphogenesis during the Caulobacter cell cycle.* Proc Natl Acad Sci U S A, 2001. **98**(7): p. 4095-100.
19. Wheeler, R.T. and L. Shapiro, *Differential localization of two histidine kinases controlling bacterial cell differentiation.* Mol Cell, 1999. **4**(5): p. 683-694.
20. Lam, H., J.Y. Matroule, and C. Jacobs-Wagner, *The asymmetric spatial distribution of bacterial signal transduction proteins coordinates cell cycle events.* Dev Cell, 2003. **5**(1): p.

149-59.

21. Reisinger, S.J., et al., *DivL performs critical cell cycle functions in Caulobacter crescentus independent of kinase activity.* J Bacteriol, 2007. **189**(22): p. 8308-20.
22. Iniesta, A.A., N.J. Hillson, and L. Shapiro, *Cell pole–specific activation of a critical bacterial cell cycle kinase.* Proc Natl Acad Sci U S A, 2010. **107**(15): p. 7012-7017.
23. Ohta, N., et al., *A histidine protein kinase homologue required for regulation of bacterial cell division and differentiation.* Proc Natl Acad Sci U S A, 1992. **89**(21): p. 10297-10301.
24. Radhakrishnan, S.K., M. Thanbichler, and P.H. Viollier, *The dynamic interplay between a cell fate determinant and a lysozyme homolog drives the asymmetric division cycle of Caulobacter crescentus.* Genes Dev, 2008. **22**(2): p. 212-225.
25. Paul, R., et al., *Allosteric regulation of histidine kinases by their cognate response regulator determines cell fate.* Cell, 2008. **133**(3): p. 452-461.
26. Gillespie, D.T., *Exact stochastic simulation of coupled chemical reactions.* J Phys Chem, 1977. **81**(25): p. 2340-2361.
27. Gonze, D., J. Halloy, and A. Goldbeter, *Deterministic versus stochastic models for circadian rhythms.* J Biol Phys, 2002. **28**(4): p. 637-653.
28. Rao, C.V. and A.P. Arkin, *Stochastic chemical kinetics and the quasi-steady-state assumption: Application to the Gillespie algorithm.* J Chem Phys, 2003. **118**(11): p. 4999-5010.
29. Domian, I.J., K.C. Quon, and L. Shapiro, *Cell type-specific phosphorylation and proteolysis of a transcriptional regulator controls the G1-to-S transition in a bacterial cell cycle.* Cell, 1997. **90**(3): p. 415-424.
30. McGrath, P.T., et al., *A dynamically localized protease complex and a polar specificity factor control a cell cycle master regulator.* Cell, 2006. **124**(3): p. 535-547.
31. Jacobs, C., et al., *Cell cycle-dependent polar localization of an essential bacterial histidine kinase that controls DNA replication and cell division.* Cell, 1999. **97**(1): p. 111-20.
32. Cai, S.J. and M. Inouye, *EnvZ-OmpR interaction and osmoregulation in Escherichia coli.* J Biol Chem, 2002. **277**(27): p. 24155-24161.
33. Deich, J., et al., *Visualization of the movement of single histidine kinase molecules in live Caulobacter cells.* Proc Natl Acad Sci U S A, 2004. **101**(45): p. 15921-15926.
34. Quon, K.C., et al., *Negative control of bacterial DNA replication by a cell cycle regulatory protein that binds at the chromosome origin.* Proc Natl Acad Sci U S A, 1998. **95**(1): p. 120-125.
35. Quon, K.C., G.T. Marczynski, and L. Shapiro, *Cell cycle control by an essential bacterial two-component signal transduction protein.* Cell, 1996. **84**(1): p. 83-93.
36. Mignot, T. and J.W. Shaevitz, *Active and passive mechanisms of intracellular transport and localization in bacteria.* Curr Opin Microbiol, 2008. **11**(6): p. 580-585.
37. Reid, B.G. and G.C. Flynn, *Chromophore formation in green fluorescent protein.* Biochemistry (Mosc), 1997. **36**(22): p. 6786-6791.
38. Jakobs, S., et al., *EGFP and DsRed expressing cultures of Escherichia coli imaged by confocal, two-photon and fluorescence lifetime microscopy.* FEBS Lett, 2000. **479**(3): p. 131-135.
39. Evdokimov, A.G., et al., *Structural basis for the fast maturation of Arthropoda green fluorescent protein.* EMBO Rep, 2006. **7**(10): p. 1006-1012.
40. Gordon, A., et al., *Single-cell quantification of molecules and rates using open-source*

microscope-based cytometry. Nat Meth, 2007. **4**(2): p. 175-181.